ELSEVIER

Contents lists available at ScienceDirect

Chaos, Solitons and Fractals

Nonlinear Science, and Nonequilibrium and Complex Phenomena

journal homepage: www.elsevier.com/locate/chaos



Intermittent event evaluation through a multifractal approach for variable density jets



Bianca Viggiano ^{a,*}, Greg Sakradse ^a, Sarah Smith ^a, Rihana Mungin ^a, Pradeep Ramasubramanian ^a, Dan Ringle ^a, Kristin Travis ^a, Naseem Ali ^a, Stephen Solovitz ^b, Raúl Bayoán Cal ^a

- ^a Department of Mechanical and Materials Engineering, Portland State University, Portland, OR 97207, USA
- ^b School of Engineering and Computer Science, Washington State University Vancouver, Vancouver, WA 98686, USA

ARTICLE INFO

Article history: Received 15 October 2020 Revised 2 February 2021 Accepted 17 February 2021

Keywords: Multifractal Turbulent jet Variable-density Octant analysis Entrainment Experimental

ABSTRACT

Variable-density jets occur in many systems, including geophysical flows and industrial applications, exhibiting a large range of scales of Reynolds and Richardson numbers. A series of jets with varying densities was ejected vertically into a large ambient region. Using particle image velocimetry, the near-exit velocity fields were measured for three different gases exhausting into air: helium, air and argon. Experiments considered relatively low Reynolds numbers from approximately 1500 to 5500 with Richardson numbers near 0.001 in magnitude. These included a variety of flow responses, notably nearly laminar, turbulent and transitioning jet flows. Flows were examined through a multifractal framework, and the singularity spectrum showed the characteristics of the flow based on the evolution in the streamwise and wall-normal direction. The variation of the Hölder exponent displayed the asymmetry and intermittency of the flow. Similar to the Reynolds shear stress, the development of intermittent behavior is a function of downstream location with respect to changes in the Reynolds number. The density of the exiting jet also influences the location of high intermittency within the flow signal. Lower density jets provide increased variability of the signal within the ambient air and the shear layer close to the exit of the jet. Specifically, the highest degree of multifractality is observed within the mixing layer of the helium jet at a transitioning Reynolds number. Conditional averaging with respect to the fluctuating velocity components and the pointwise Hölder exponent reveals high velocity-intermittency interactions at the inside of the jet mixing layer when fluid is entrained and at the turbulent/non-turbulent interface when fluid is ejected. Finally, line integral convolution illustrates the impact of turbulent/non-turbulent interface on the jet dynamics.

© 2021 Elsevier Ltd. All rights reserved.

1. Introduction

Turbulent jets are important fundamental flows with broad applications [1] and relevant examples are found in industrial applications such as smoke stack emissions, as well as an array of geophysical features including underwater hydrothermal plumes, volcanic ejections, and geological sedimentation [1,2]. Through examination of turbulence development and entrainment, more accurate plume and eruption models may be generated, helping to predict downstream behavior [3–5].

Previous studies characterize jet flow dynamics in relation to Richardson and Reynolds numbers, examining shear layer formation and entrainment. Buoyant jets, where jet density is less than

* Corresponding author. E-mail address: viggiano@pdx.edu (B. Viggiano). that of the ambient fluid, show increased turbulence development in the near-field region compared to higher density jets [6]. Studies have shown that entrainment is pronounced in buoyant jets [7-9]. A numerical study of by Wang et al. [10] compared jets of helium, air and CO2 into air, finding the lower-density jet developed more quickly than the denser jet. Similar trends were confirmed through experimental campaigns [11,12]. Gharbi et al. [11] used laser Doppler velocimetry to examine jets of helium and CO₂ with the same exit momentum flux exhausting into a coflow. The study found rapid development of turbulence for the helium in comparison to the carbon dioxide jet. Viggiano et al. [12] considered gases of variable densities ejected from a constantdiameter jet, showing more rapid flow development and prominent Reynolds stresses with low-density jets. In addition, more significant fluctuations were observed within the first few diameters when exit Reynolds numbers were transitional, corresponding to

high entrainment of ambient air. The far-field effects of variable density jets were examined by Gerashchenko and Prestridge [13], finding that the density gradient heavily influenced the turbulent kinetic energy (TKE) of the jet. The larger gradient leads to increases TKE as a function of streamwise distance from the jet while the small gradient flow causes the TKE to decrease as the jet develops downstream. In a particle tracking experimental study by Wolf et al. [14], the local entrainment velocities were found to be dependent on the local shape of the jet interface with the ambient fluid. The shape and interactions across the mixing layer are formed by the size of the eddies present at the interface, suggesting that entrainment can be quantified through the characterization of small scales of turbulent interface motion. A comparable, more granular examination of entrainment phenomena with buoyant jets in the near field region may grant perspective on bulk behavior as the jet continues to develop downstream.

One such analytical technique is multifractal analysis, used to characterize the self-similar nature of roughness [15]. The self-similarity of turbulent energy scales, as described by Kolmogorov [16], allows for examination of turbulent flows through a multifractal framework [17]. Foundational work by Meneveau and Sreenivasan [18] permitted an energy cascade model with regards to dissipation of turbulence kinetic energy through multifractal analysis. A fractal signal is characterized by the power law. When homogeneous, it is classified as monofractal, while when multifractal, it is heterogeneous. A multifractal field is described by a continuum of scaling exponents and results in numerous criteria that describe the nature of the signal.

Several approaches to the quantification of the multifractal parameters have been established over the years. Russell et al. [19] defined the box-counting method for approximation of the fractal dimension and in turn the multifractal spectrum. The signal is meshed into various box sizes, r, and a normalized measure is then computed. For random phenomena, fractal analysis based on fractional Brownian motion (fBm) methods is often utilized. Fractal Brownian functions (fBfs), a generalization of fBm, are the most encountered physical models [20]. This technique results in a fractal dimension that is invariant with transformations [21]. Eke et al. [22] defined the signal summation conversion (SSC) method, which can be applied to stationary and non-stationary time series alike. Finally, the multifractal wavelet method, introduced by Jaffard et al. [23], is a robust technique which divides the signal into wavelets that show a zero-mean, fast-decaying waveform.

Multifractal formalism has been extended to describe flow characteristics in turbulent free-shear jets for both numerical and experimental data [24–27]. Sykes and Gabruk [25] used numerical data of a jet to determine fractal dimension through areaperimeter and box-counting analyses. Lane-Serff [24] experimentally investigated buoyancy affects of a downward-oriented jet on the fractal structure and dimension. Seo and Lyu [26] examined jet turbulence intensity and dilution using the box-count method over a two-dimensional space, finding that multifractal properties can be used to characterize the discharge outfall. López et al. [27] applied a gliding box method to turbulent axisymmetric plumes, revealing that the time evolution of the plume and momentum flux are able to be characterized by multifractal parameters.

Although the application of multifractal analysis in turbulent flow is well established, this technique has not been applied for investigation of entrainment in buoyant free-shear flow. This method provides small scale information from signals which are highly intermittent and therefore cannot be well-described via more standard statistical approaches. The explicit relationship between the fluctuating temporal signal and the flow singularities, resulting from multifractal formalism, provides an idea of the type of roughness and strong nonuniformities of the flow. This provides an alternative/extension beyond typical entrainment analysis descriptions

to give details of the locations within the shear layer where intermittency is dominating [28,29] and how it is affected by the density of the jet. More specifically, building on the work of Viggiano et al. [12], this study aims to apply multifractal analysis to characterize the influence of varying Richardson and Reynolds numbers on jet entrainment. The resulting fractal parameters can quantitatively describe the existence of intermittent behavior at the turbulent/non-turbulent interface through the presence of the active flow features. In addition, the line integral convolution (LIC) technique of post-processing will be applied to visualize the flow behavior. This method provides a more tangible representation of the spatial interactions between multifractal and statistical parameters in relation to fluctuations of the velocity. The multifractal framework and LIC theoretical methods are presented in Section 2. The experimental setup, data collection techniques, and details of the dataset are given in Section 3. The application of the analysis techniques and discussion follow in Section 4, and concluding remarks on the implications with respect to turbulent development are given in Section 5.

2. Theory

2.1. Multifractal formalism

2.1.1. Focus-based multifractal signal summation conversion analysis

Multifractal formalism allows for analysis through the detection of singularities while scaling to identify self-similarity within the signal [15,30–33]. Application of a scale-dependent power law considers a statistical measure, μ , such as flow velocity and energy dissipation, through application of a fractal scaling power law exponent β .

$$\frac{\mu(t,s_2)}{\mu(t,s_1)} = \left(\frac{s_2}{s_1}\right)^{\beta},\tag{1}$$

where s_1 and s_2 are scales which determine respective time windows. The degree of singularity in μ can be assessed through the Hölder trajectory [30] as

$$\mu(t,s) \propto s^{h(t)}$$
. (2)

Through the signal summation conversion analysis, a series of parameters are evaluated in order to obtain the Hölder exponent [30]. First, the implementation of a scaling function,

$$S_{\sigma}(q,s) = \left\{ \frac{1}{N_{S}} \sum_{i=1}^{N_{S}} \left\{ \frac{1}{s-1} \sum_{k=1}^{s} ({}_{bd}Y[(i-1)s+k] - \langle {}_{bd}Y_{i} \rangle)^{2} \right\}^{q/2} \right\}^{1/q},$$
(3)

allows for the Hurst exponent, H(q), to be extracted from its regression. Here, q is the order and N_S is the number of temporal windows. The cumulatively summed signal is bridge detrended, producing $_{bd}Y$, in each window of the centered signal profile, Y. Specifically, this indicates that prior to calculating the standard deviation in each window, a "bridge", or line, connecting the first and last points within the window is removed. Using the focus-based multifractal approach, the best fit is found through convergence of the least sum of squared errors [30],

$$SSE = \sum_{q} \sum_{s} \left[\log S_{\sigma}(q, s) - H(q) \cdot (\log s - \log L) - \log S_{\sigma}(L) \right]^{2},$$
(4)

where L is the largest scale. The Hurst exponent is related to the scaling function as follows,

$$S_{\sigma}(q,s) \propto s^{H(q)},$$
 (5)

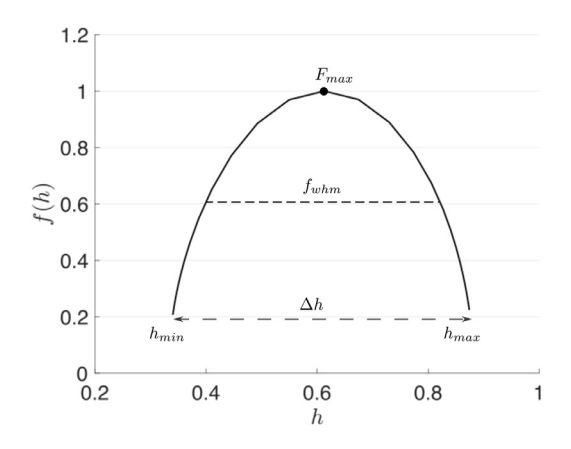


Fig. 1. Theoretical multifractal singularity spectrum.

and allows for examination of the length of the memory of the signal. This serves as a measure local multifractality. Given H(q), the multiscaling exponent is defined as

$$\tau(q) = q \cdot H(q) - 1. \tag{6}$$

The Hölder exponent is then defined as the slope of the tangent line of the scaling exponent taken with respect to q, which is $h = d\tau(q)/dq$, yielding the singularity spectrum,

$$f(h) = \inf_{q} (q \cdot h - \tau(q)). \tag{7}$$

The singularity spectrum produces multiple measures of the degree of multifractality, as shown in Fig. 1.

2.1.2. Pointwise Hölder exponent

The pointwise Hölder exponents identify features of the flow field through analysis of single-point time-series measurements [34]. This pointwise parameter measures the regularity of the signal by approximating it to the polynomial as,

$$p_T(t) = \sum_{i=0}^{m-1} \frac{u_{j,k}^i(T)}{i!} (t - T)^i,$$
 (8)

where T is the position in time, and m is the total number of instances that the velocity, u, is differentiable in a neighborhood, δ , about T. Given the 2-D experimental data, a point by point analysis is performed with respect to the physical location j,k of the velocity signal through time.

The pointwise Hölder exponent, $\alpha_{j,k} \equiv \alpha(u_{j,k}) \geq 0$, exists given that

$$|u_{i,k}(t) - p_T(t)| \le K|t - T|^{\xi},$$
 (9)

where the constant, K > 0. Therefore $\alpha_{j,k}$ at T is based on the least upper bound of ξ fulfilling Eq. (9). The pointwise Hölder exponent can be approximated based on the log-log regression of the oscillations of the signal:

$$O_{T\pm\delta} = \max[u_{j,k}(t \in \{T - \delta, \dots, T + \delta\})] - \min[u_{j,k}(t \in \{T - \delta, \dots, T + \delta\})],$$

$$(10)$$

within a distance δ of the position T, where δ is a logarithmically-distributed set of bins. The pointwise Hölder exponents can be considered as a measure of intermittency (singularity) of the signal. So, the main goal of analysing the pointwise Hölder exponents is to determine the temporal correlation between the intermittency and velocity. These correlations are quantified through the conditional averaging.

2.1.3. Conditional averaging

Quadrant analysis is a conditional averaging technique commonly used with wall-bounded jets to classify flow events based on the sign of the fluctuating velocity components. The streamwise (u') and spanwise (v') fluctuating velocities are found via Reynolds decomposition (i. e. $u' = u - \overline{u}$ where u is the instantaneous velocity signal and \overline{u} is the time-averaged velocity). Past studies of near-wall flow gave rise to the nomenclature of sweeps and ejections [35] to describe the anti-correlated fluctuations, which are typically the largest contributors to the Reynolds stress [36,37]. For application to a vertically-oriented free-shear jet, Viggiano et al. [12] introduced new terminology for quadrant analysis to more appropriately describe the events for the right half of a quasisymmetric jet. The quadrants are defined as Q1: advancing-flow ejections (u' > 0 and v' > 0), Q2: advancing-flow entrainment (u' > 0) 0 and v' < 0), Q3: impeding-flow entrainment (u' < 0 and v' < 0) and Q4: impeding-flow ejections (u' < 0 and v' > 0), on a Cartesian plane whose abscissa is v' and ordinate is u'.

Keylock et al. [38] expands a method based on quadrant analysis where the conditions are dependent on a velocity component and multifractal behavior associated with the velocity. This allows for the consideration of the velocity-intermittency relations by implementing the conditional averaging with respect to fluctuating streamwise velocity, u', and fluctuating pointwise Hölder exponent, α' . Following the nomenclature presented by Viggiano et al. [12] for the right half of a free-shear jet, this study extends the method introduced by Keylock et al. [38] to include the fluctuating spanwise velocity component, v', to characterize signal dynamics as they relate to entrainment. The flow is conditioned into eight events, octant analysis, based on the sign of the three fluctuating quantities as presented in Fig. 2 as employed for a wind turbine array boundary layer [39,40]. Only the right half of the jet is included as the signal conditioning for entrainment dependents on the sign of the transverse fluctuations. Investigation of the fluctuations of the velocity components and the associated pointwise Hölder exponents give insight into the relationship between the velocity and the scaling of the velocity increment [38,41]. A time series with a single fractal dimension will result in a constant Hölder regularity. However, a multifractal signal will have a pointwise Hölder exponent that depends on the existence of active flow features, and therefore it varies. The sign of the Hölder exponent reveals the signal dynamics, a rough signal presents negative fluctuations, $-\alpha'$ while a smoother signal corresponds with $+\alpha'$. The regions of the mixing layer with large correlations between $-\alpha'$ and -v' gives knowledge of where increased intermittency is the driving mechanism of the entrainment within the jet. Characterization of the intermittent nature of the temporal signal (chaotic regions of the mixing layer) provides entrainment and ejection knowledge. The temporal dependence of intermittency, visualized by the pointwise Hölder exponent fluctuations, could be integral for three-dimensional modeling of plume dynamics. For example, the Active Tracer High-Resolution Atmospheric Model (ATHAM) requires an involved treatment of the turbulent quantities of the jet in order to capture accurate plume characteristics [42]. One of these quantities, the plume development through time, could be benefited through increased knowledge of the temporal mulifractal behavior, i.e., the pointwise Hölder exponent trends within the mixing layer.

2.2. Line integral convolution

First introduced by Cabral and Leedom [43], LIC is an image processing method that allows for qualitative study of two and three-dimensional vector fields. The visualization technique uses linear and curvilinear filtering techniques to locally blur textures along a vector field, which makes it capable of rendering detail

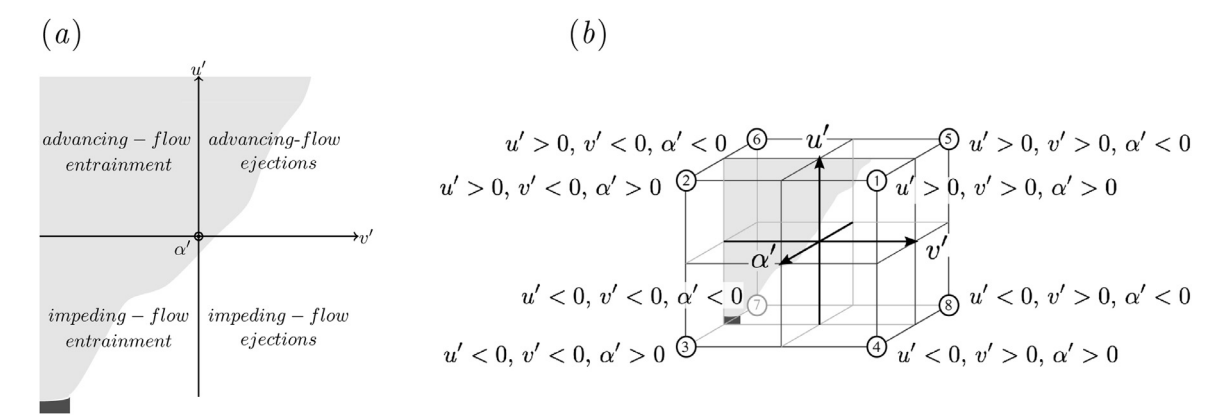


Fig. 2. Eight octants in two-dimensional (a) and three-dimensional (b) representations are shown for the right half of a vertically-oriented jet. The flow is condition by the fluctuating streamwise velocity (u'), spanwise velocity (v') and pointwise Hölder exponent (α').

on intricate dense vector fields. Other vector visualization algorithms, such as streamlines and particle tracing techniques, depend on placement of the particle or streamline sources, and therefore eddies in the vector field can be missed. LIC is a more robust visualization technique, as it is independent of the particle placement and source [44].

The algorithm inputs are a vector field and a texture comprised of white noise data with the same resolution as the vector field. Applying this method to experimental data, unit vectors of the measured velocity field are used to compute streamlines starting from a given data point in space. The analysis method provides streamlines based on vector direction, which are independent of magnitude. Line integral convolution has been used by Urness et al. [45] to image PIV measurements of hairpin shaped vortices in turbulent boundary layers. Additionally, color weaving was used to differentiate the LIC textures with further scalar quantities. In the work of Matvienko and Krüger [46], spectral frequencies defined by LIC filtering techniques show promise in processing speed and image detail. This frequency-controlled approach is useful when considering how localized flow properties change with variable densities.

Implementation of this analysis on turbulent jet flow increases the visibility of interactions between the jet fluid and ambient air. Further, post-processing techniques can be used to include the magnitude of the velocity, areas of high stress and direction of the flow without decreasing the clarity of the streamlines. The algorithm is provided in Appendix A.

3. Experimental setup

Experiments were conducted with a vertical pipe apparatus at Washington State University Vancouver, shown schematically in Fig. 3(a). Compressed gas is directed vertically upward out of a 305 mm long, constant diameter pipe to create a jet in ambient air. The jet exit diameter is 11.84 mm with a non-dimensional pipe length of 26, which exceeds classic criteria for fully developed turbulent pipe flow [47]. In addition, flow measurements at the exit display a log-law profile. The static temperature and pressure are monitored upstream of the exit with a T-type thermocouple and gage pressure transducer, respectively. Fig. 3(b) shows the coordinate system for the jet, which has been oriented to agree with the convention of previous jet studies. Here, the vertical axis (streamwise direction) is x and the horizontal axis (spanwise direction) is y.

Three different compressed gases are used for the jets: helium, air and argon. The fluid exits the pipe normal to a horizontal plate in the center of a laboratory, where the jet exit is located hun-

Table 1 Experimental test conditions.

Medium	Exit velocity [m/s]	Viscosity $(\times 10^{-5})$ [N s/m ²]	Density [kg/m³]	Re	Ri (×10 ⁻⁵)
He1460	14.4	1.96	0.167	1460	350
He2800	27.7	1.96	0.167	2800	94
He5520	54.5	1.96	0.167	5520	25
Air	4.99	1.82	1.21	3910	0
Argon	3.59	2.23	1.66	3175	-250

dreds of diameters away from any wall. The jet is seeded by a Laskin nozzle atomizer, that produces approximately 1 μ m olive oil droplets. This combination of seeding and atomizer provides good scattered light intensity and size of particles [48]. The apparatus is operated at a constant exit speed for several minutes to achieve a uniform tracer distribution near the exit of the jet. Ambient air seeding is provided by a fog generator in the laboratory, which produces micron-scale aqueous glycol droplets with a similar density to the olive oil. Background speeds in the ambient are typically less than 1 mm s⁻¹.

The flow is studied with a commercial PIV system. The dual head lasers emit a pair of closely timed pulses, each with 50 mJ energy and 532 nm wavelength, which illuminate the droplet tracers. The pulses are converted to laser sheets of approximately 0.5 mm thickness using a diverging cylindrical lens and a converging spherical lens. The sheet is oriented vertically and aligned to the centerline of the jet. The instantaneous tracer distribution is imaged with a 1.4-megapixel digital camera aligned perpendicular to the laser sheet. Pulses are spaced approximately 10 µs apart when studying the centerline flow and approximately 200 µs apart when examining the ambient flow. These times were selected to accurately capture the local responses with optimal PIV accuracy [49]. Pivlab2000 is used to process all PIV images to determine the instantaneous, two-dimensional velocity field [50].

Five testing conditions were considered, as listed in Table 1. In later discussion, each case is identified by the medium given in the table. The exit velocity of the jet was varied, as well as the medium, obtaining a variety of Reynolds numbers and Richardson numbers. The Reynolds number and Richardson number are formulated for the jet as, $Re = \rho_j U_j D/\mu_j$ and $Ri = g(\rho_a - \rho_j) D/(\rho_j U_j^2)$, respectively. Here, ρ_j is the jet density, U_j is the exit velocity, D is the exit diameter, and μ_j is the jet viscosity. The gravitational acceleration is denoted as g, and the ambient air density $\rho_a = 1.21 \, \text{kg/m}^3$. The buoyant cases, utilizing helium as the jet medium, spanned exit conditions from nearly laminar to fully developed turbulent flow. These helium jet cases have Reynolds num-

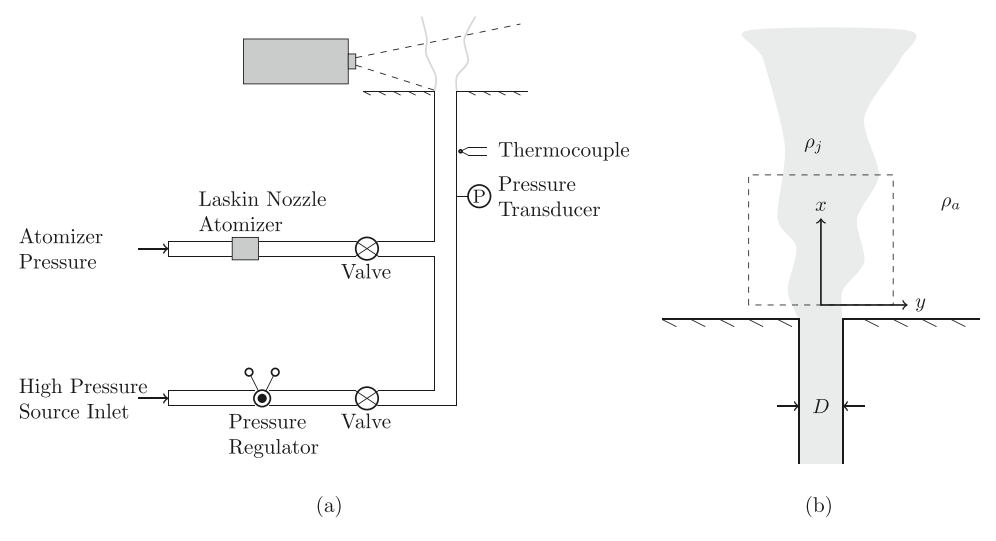


Fig. 3. Schematic of experimental apparatus (c.f. Viggiano et al. [12]).

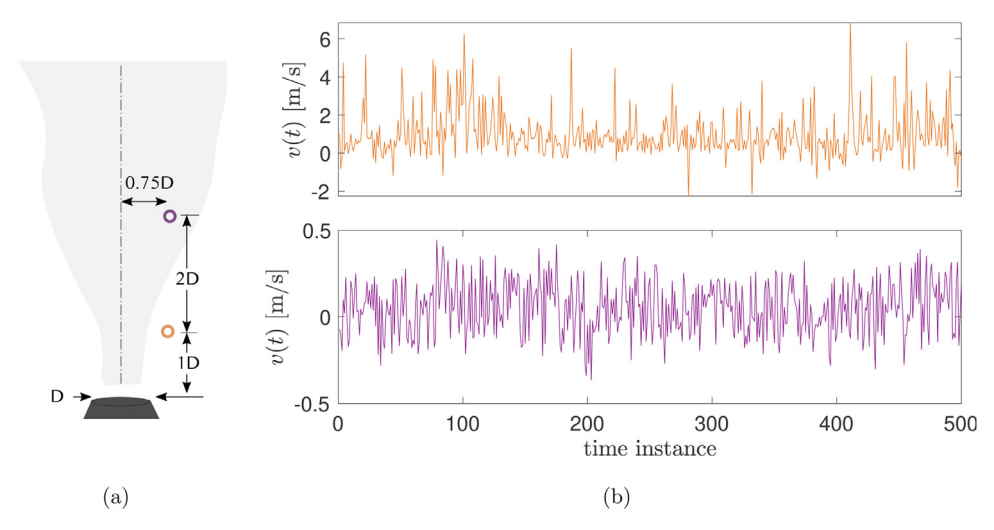


Fig. 4. The raw temporal signal of instantaneous velocity for He2800 at two locations within the jet at y/D = 0.75, x/D = 1 shown in orange (top) and at y/D = 0.75, x/D = 3 presented in purple (bottom). (For interpretation of the references to color in this figure legend, the reader is referred to the web version of this article.)

bers ranging from 1460 to 5520 and Richardson numbers between 350×10^{-5} to 25×10^{-5} . The air and argon cases were chosen to observe effects of the exit fluid density, from a buoyant to non-buoyant to negatively buoyant jet. Their *Re* values are in the intermediate range of the helium cases, corresponding most closely to the transitioning flow. The first four downstream diameters of the jet are examined, allowing for analysis to be performed on the near exit, development region for all cases. A total of 500 time instances were captured for each case. The experiments were repeated to validate the results and were within the uncertainty. Reference Viggiano et al. [12] for further detail on the experimental procedures.

4. Results

4.1. Multifractal analysis

First, the time instances of the instantaneous velocity of He2800 at two locations within the jet are provided in Fig. 4 to visualize differences in the fractal behavior of the jet. The two signals are taken at y/D = 0.75 for two downstream locations of x/D = 1, the top panel (orange), and x/D = 3, the bottom panel (purple), see schematic in Fig. 4(a). Nearer the exit of the jet, at

y/D = 0.75, x/D = 1, the signal presents typical characteristics of a fluctuating velocity with correlations occurring over a scale of around 40 time instances. As the jet develops, at x/D = 3, the purple curve appears to show less extreme events, which would lead the observer to believe that the fluid is less intermittent at that location, but the rough signal contains multifractal characteristics, as will be see in the following sections.

4.1.1. Multifractal singularity spectrum

Fig. 5 contains the singularity spectra for the transitioning helium case, He2800, where the Hölder exponent h presents the singularity of the temporal signal of velocity. Two locations within the jet are presented, x/D=1 and 3, at y=0.75D. For the FMF-SSC analysis, a range of $q\pm 15$ is used to evaluate the Hölder exponents and the input scale s has an initial value of 8 time steps as a minimum and the total signal length as a maximum (500 snapshots). The spectrum lies between $0.45 \le h \le 0.9$ at the upstream location and shifts to $0.5 \le h \le 1.1$ when x=3D. Large scale dynamics cause the Hölder exponent to be above 1 for the x=3D signal [12]. The right tail of the spectra also moves down at the farther downstream location. The decrease in the minimum value of h signifies the flow is less complex at the x=1D location [26]. Further, the increase in the degree of multifractality, the width of

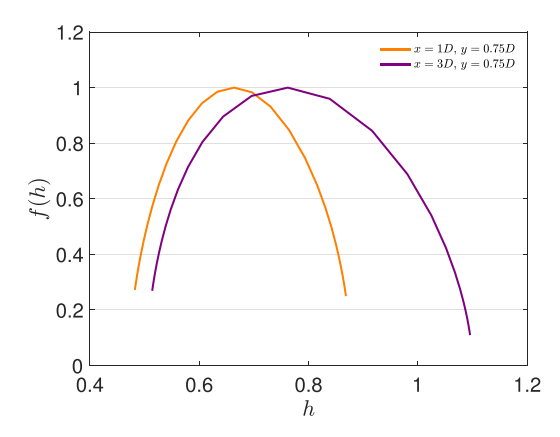


Fig. 5. The singularity spectrum for He2800 at y/D=0.75 for two downstream locations of x/D=1 and x/D=3. The Hölder exponent, h, indicates singularities of a local temporal signal while the width of the spectra, Δh , informs on the degree of intermittency at a given location through time.

the spectrum Δh , indicates increased intermittency at the farther downstream location.

To facilitate the investigation of all (x, y) locations, contours of the degree of multifractality, Δh are shown in Fig. 6. When describing the PIV data, the degree of multifractality illustrates the variability of the flow field through time as a function of spatial location. He1460 contains a smooth signal of uniform width throughout the field of view. Small pockets of increased degree of multifractality form at $x/D \sim 3$ along the outside of the core, signifying that the jet may be starting to transition to a turbulent regime. He2800 shows a jet that expands in the spanwise direction as it grows downstream, where intermittency is minimal. Along the outside of the jet an increase in complex structures form in the downstream direction, beginning at $x \sim 1.5D$, where increased mixing between the jet fluid and ambient air is occurring as it transitions to turbulent flow. After transitioning, He2800 presents the highest variability of flow features within the mixing layer, reaching $\Delta h \sim 0.83$. There also exists increased Δh within the center of the jet on the inside of the mixing layer for x/D > 2.5. The fully turbulent jet of He5520 expands in width as *x* increases, similar to He2800, but the effects are more pronounced. Here, increased complexity of the eddies at the turbulent/non-turbulent interface occurs directly following the jet exit, signifying that the turbulent exit flow results in significant variation upon contact. Because the jet expands beyond the spanwise bounds of the field of view, highly intermittent behavior is only observed from 0 < x/D <2.5. It is probable that the Δh structures follow the outside of the mixing layer, similar to those seen in the transitional case. The increased multifractality present in the He2800 case is not observed in the He5520 case and could be due to the more significant turbulent fluctuations present when compared to the fully turbulent jet [12], indicating that the multifractal behavior is not in some way proportional to Re.

The neutrally buoyant jet of air shows a distinct transformation from the simple turbulent flow structures inside the jet and mixing layer to a more complex region outside the jet. Similar to He5520, the high intermittency structures begin immediately after the ejection of the jet. Finally, the argon jet presents a smaller core, but again there is a well-defined interface from inside the shear layer, with a large gradient in scale complexity. The argon jet is unique: all other cases show increased variability structures lining the edges of the jet, which quickly dissipate to simpler flow features within the ambient air regions. However, with argon, increased levels of Δh are observed along the outside of the jet and the ambient air. There also exists a small pocked of increased Δh within the core of the jet near x = 3D, similar to the transition

helium case, He2800. The Reynolds number dependence appears consistent with previous observations [12], as Re increases the intermittent behavior begins nearer the jet exit. The trends seen in air and argon are not comparable to the helium jets, signifying that presence of multifractality is also related to the Richardson number, i.e., buoyancy of the jet. This is observed through the increase in structures present near the exit of the jet, as well as outside of the mixing layer. Increased variation of multifractality observed within the ambient for the argon case can be in part due to the increased inertia of the argon. Increased Δh values near the exit of air and argon are more similar to the fully developed helium case, He5520, although the jets of air and argon do not spread as quickly within the region of interest.

4.1.2. Velocity-intermittency conditioned octant analysis

Octant analysis is performed on the five cases. The velocity-Hölder regularity interaction, $\langle u'v'\alpha'\rangle$, is conditioned into eight events based on the sign of the fluctuating streamwise velocity, the spanwise velocity and the Hölder exponent. Due to differences in the magnitude of the variables, the parameters have been normalized using their respective standard deviation. The results are shown in Fig. 7. Given that octants 2, 4, 6 and 8 (quadrants 2 and 4) show negligible contributions, shown in Viggiano et al. [12], only octants 1, 3, 5 and 7 (quadrants 1 and 3) are presented here. From Section 2.1.3, recall that O1 (u'>0, v'>0 & $\alpha'>0$) and O5 (u'>0, v'>0 & $\alpha'<0$) indicate advancing-flow ejections while O3 (u'<0, v'<0 & $\alpha'>0$) and O7 (u'<0, v'<0 & $\alpha'<0$) indicate impeding-flow entrainment. Within each quadrant of interest, the flow field is conditioned further by $\pm\alpha'$ to indicate the signal variability.

The near laminar case of helium shows minimal instances of intermittency in the flow field. There is an increase in $\langle u'v'\alpha'\rangle$ in O5 near the end of the field of view, similar to the increase in multifractality seen in Fig. 6. He2800 presents structures that highlight the turbulent development of the jet in O5 and O7. The location of high intermittency is dependent on the mechanism of the flow field. The advancing-flow ejections, O5, show a rough signal present within the mixing layer, extending spanwise to the turbulent/non-turbulent interface, while the increased intermittency is observed within the jet for quadrant 3, representing impeding-flow entrainment. The feature present in O5 develops near x/D = 1.5 and extends from 0.3D to 1.1D in the spanwise direction at the end of the field of view with a peak $\langle u'v'\alpha'\rangle$ value of 0.83 observed. Positive pointwise Hölder exponents show minimal change across the mixing layer for all quadrants. The turbulent case of helium shows similar trends as He2800 with the exception that the features present in O5 develop immediately following the jet exit and reach a maximum magnitude of \sim 1.45. The structure also extends past the field of view in the spanwise direction from $\sim 0.4D$ to y > 1.2D at x=2D and beyond. The location of high intermittency in O7 shows similar trends to He2800, tracing the outside of the jet core. These structures are nearly constant in magnitude as the jet develops downstream. He2800 and He5520, which are positively buoyant, show increased interaction between the ambient and jet fluids to create a structure in O5 that grows quickly in the spanwise direction once turbulence is present.

The rough signal, high intermittency features are again observed in the $-\alpha'$ octants for air, with minimal contributions from 01 and 03. The advancing-flow ejections, 05, show the presence of increased velocity-intermittency interactions at the interface of the mixing layer and the ambient air, similar to He2800 and He5520. The structure shows nearly constant magnitude as it develops downstream, reaching a maximum of 0.95. Compared to the transitioning and turbulent helium cases, the air shows minimal expansion in the spanwise direction as x increases. In 07, the structure

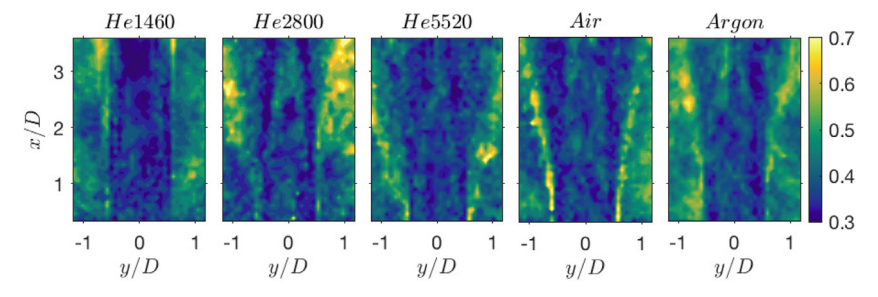


Fig. 6. The degree of multifractality, Δh , for all cases.

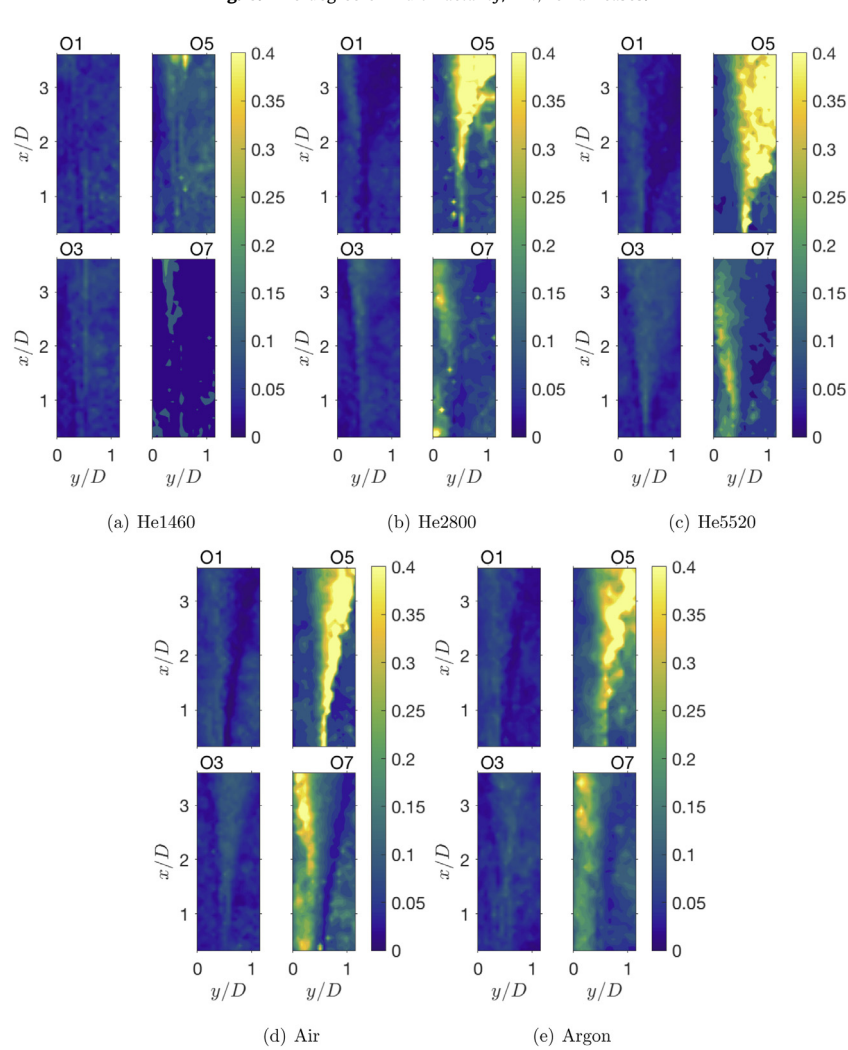


Fig. 7. Octant analysis of $\langle u'v'\alpha' \rangle$. Four octants are shown for clarity, O1, O5, O3 and O7, for all considered cases.

following the inside of the shear layer is distinct and greater in magnitude than the events seen in O7 for He2800 and He5520.

The structure in O5 for argon exhibits a similar formation and magnitude when compared to air, however, the region is not uniform in shape and peaks in value at 0.68, much lower than the air case and He2800. Due to the increased density of the ejected gas (Ri < 0) the fluid appears to have greater inertial effects compared to the neutrally (Ri = 0) and buoyant gases (Ri > 0). This enables increased interplay between the ambient air and the argon jet, which creates a wave-like structure at the outsides of turbulent/non-turbulent interface, and in turn, rough signal dynamics within the ambient air. For O7, impeding-flow entrainment, the feature is lacking in magnitude and coherence when compared

with the air case. Although the feature is less coherent, it shows development that is independent of y in the test field of view, which is unique.

All cases show a low-magnitude structure within the mixing layer in O3, indicating a smoother signal is present within the mixing layer for impeding-flow-entrainment. This structure connects the high intermittency interactions between the inside of the jet with the structures along the outside of the jet. More specifically, the regions where the flow is pulled into the high-speed core to where the ejections from the mixing layer interact with the quiescent ambient air.

Line integral convolution is applied to a single instant in time for the visualization of the turbulent/non-turbulent interfacial in-

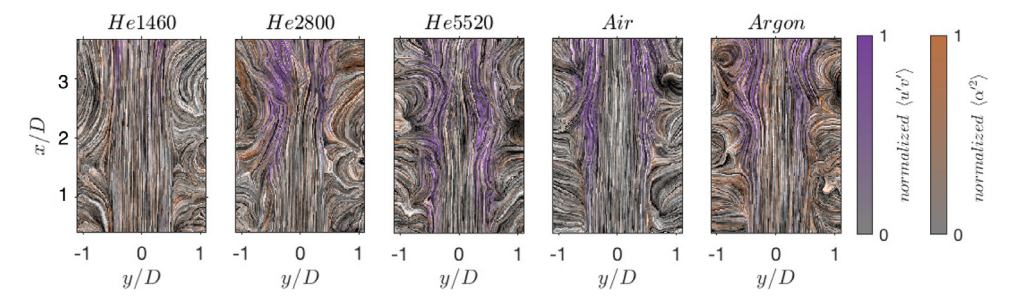


Fig. 8. Line integral convolution of a single snapshot of velocity fluctuations for all cases. Each convoluted image is colorwoven with the respective $|\langle u'v'\rangle|$ and $\langle \alpha'^2\rangle$, normalized to a unit interval, for each case.

teractions of instantaneous velocity, and the results are presented in Fig. 8. The implementation of LIC on the free-shear jet flow increases the visibility of the streamlines within the jet as well as in the ambient air. Post-processing of the images is performed to increase the contrast and to include the colorweaving of the $|\langle u'v'\rangle|$ in purple and $\langle \alpha'^2\rangle$ in orange, normalized over a unit interval for each respective case. Only negative fluctuations of the pointwise Hölder exponents are considered to examine regions of high intermittency.

The near laminar case of helium shows relatively large sweeping eddies along the outside of the uniform jet. He1460 contains minimal Reynolds shear stresses [12] and inconsequential contributions from the pointwise Hölder exponent when compared with the other cases. Therefore, via normalization, $\langle \alpha'^2 \rangle$ appears throughout the field of view. This is attributed to negligible intermittency present and is therefore not discussed further. The Reynolds shear stress increases in magnitude near the outside of the jet at $x/D \sim 3$, again signifying that the jet may be starting to exhibit turbulent behavior at the farthest downstream regions of the test section. The transition into turbulent flow for He2800 is seen by the increase in $|\langle u'v'\rangle|$ and $\langle \alpha'^2\rangle$ near x=1.5D. At this location, the jet begins to contort, and there is an increase in ambient air interaction with the core. Here, increased levels of intermittent behavior are observed along the outside of the high Reynolds shear stress regions. He5520 shows turbulent behavior within the entire test field of view. The ambient air is mixing with the jet starting from x < 1D. High values of the Reynolds shear stress and increased intermittent levels occur at the same locations. There are interactions between the ambient air and the jet within the shear layer, with only trace amounts of $\langle \alpha'^2 \rangle$ present outside of

The neutrally buoyant jet of air shows comparable features to those of the He5520 case, yet the characteristics are dampened. For example, the areas of high Reynolds shear stress and $\langle \alpha'^2 \rangle$ develop slightly farther downstream near x/D = 1.5 and do not traverse the spanwise direction to the same extent, but the locations of $\langle \alpha'^2 \rangle$ and $|\langle u'v' \rangle|$ in the shear layer and interactions between the ambient air and the jet are similar. The case of argon is unique as it is a negatively buoyant jet and therefore the Richardson number is negative. The convolution highlights the interplay between the jet and ambient fluids, showing the near horizontal streamlines present in the ambient air near the exit of the jet. This particular interaction creates locations of high intermittency that extend beyond the shear layer in the spanwise direction. Further, there exists pockets of $\langle \alpha'^2 \rangle$ within the jet. This behavior relates closely to the transitioning jet of He2800, although for argon, the development of $\langle \alpha'^2 \rangle$ begins almost immediately after the ejection of the jet, prior to the regions of high stress development.

Through LIC, the interactions at the turbulent/non-turbulent interface can be visualized and compared between the five cases. While He1460 shows large sweeping eddies that touch the outside of the jet, these do not interfere with the structure of the jet core

as their intensity is negligible. The largest interaction between the ambient air and the jet is observed within He2800, as it transitions at $x \sim 1.5D$. Here, eddies of all sizes penetrate the jet and create discontinuous lines within the center of the jet. The presence of varying eddies surrounding the jet is also observed in the fully turbulent jet of He5520. Although the jet is affected by the ambient air starting near the nozzle exit, the resulting contortion to the streamlines is less intense than that observed in He2800. Air and argon also show eddies that span the entire jet in the streamwise direction, but both show more uniform-sized eddies that prod the edges of the jet and create wave-like streamlines in the shear layers. All cases show that the interaction with the ambient air is prevalent enough to affect the mechanics of the jet, with the exception of He1460. Argon, the most dense gas used as a jet, is unique, showing near horizontal interactions with the ambient air near the exit of the jet. Argon is the only case that contained regions of high intermittency outside of the mixing layer in O3 as shown in Fig. 7.

5. Discussion and conclusions

Particle image velocimetry data were collected for five jet cases to examine the multifractal characteristics and entrainment behavior due to varying Reynolds and Richardson numbers. The three helium cases showed that the shear layers contained the highest degree of multifractality, corresponding well with the region of the highest Reynolds shear stress. More specifically, the area of increased Δh values develops closer to the exit of the jet with increasing Reynolds number. Air and argon displayed increased complexity nearer the exit of the jet when compared with He2800, signifying that level of buoyancy of the jet impacts the areas of increased variability of the flow structures within the field.

Mechanics of the signal were examined by conditioning $\langle u'v'\alpha'\rangle$ into octants based on the velocity components and sign of the pointwise Hölder exponent. All cases showed negligible contributions from $+\alpha'$. With the exception of He1460, distinct trends were observed between the structures present in O5 and O7. The advancing-flow ejections, O5, contained high intermittent behavior at the turbulent/non-turbulent interface and within the mixing layer while impeding-flow entrainment, O7, showed high $\langle u'v'\alpha'\rangle$ values along the inside of the mixing layer. The dependence on Reynolds and Richardson number is highlighted by conditioning the flow into octants. With respect to Re, the three cases of helium were compared. In O5, the low Reynolds number helium jet showed negligible features. For the transitioning case, a coherent feature forms within the mixing layer near x/D = 2. Finally, as the Reynolds number increases and the jet becomes turbulent, a structure that is similar in shape to that present in He2800 forms near the ejection site, showing a dependence in downstream development of intermittent behavior with respect to the Reynolds number. The buoyancy of the jet also affects the $\langle u'v'\alpha'\rangle$ values within the field of view. The shape of the structures present in He2800

contrast with those seen in the air and the argon cases. The jet of air creates a distinct, high magnitude feature in O7 that is not observed in the helium cases. Argon shows a less defined area of high intermittency in O7, which is present within and outside of the shear layer.

Near the jet exit, the differences in density of the jet plays a role in the dynamics of the signal with respect to spatial location. Helium is lighter than the ambient air and due to its reduced inertia shortly after exiting the jet, high shearing within the mixing layer is present, and in turn, increased intermittent behavior. In contrast, argon is heavier than the ambient fluid which leads to increased inertia of the fluid after ejection. This is seen by the increased levels of multifractality and stress present within the ambient air for the argon case. The effects of the ejecting fluid buoyancy presented in the study show intricate multifractal dynamics within the near-field of the jet which may not be fully characterized with the simpler one-dimensional modeling of plume dynamics [51]. Optimal predictions of buoyancy driven volcanic behavior may require more complex turbulence models [42] to accurate capture entrainment mechanics.

Finally, the application of LIC provided visualization of the streamlines of the fluctuating velocity and the spatial relationship between the Reynolds shear stress and the pointwise Hölder exponents. He2800 shows the largest interactions between the jet core and the ambient air, which correspond to areas of high Reynolds shear stress and $\langle\alpha'^2\rangle$. The turbulent case of helium and air show similar trends with respect to locations of the shear stress and pointwise Hölder exponent, although He5520 displayed increased eddies and subsequent wave-like streamlines within the jet core. Argon also shows ripples within the jet core similar to He5520, but with high $\langle\alpha'^2\rangle$ values directly following the jet ejection as well. The effects of the negatively buoyant jet are illustrated by the horizontal streamlines lining the jet core and increasing the complexity of the flow from the jet exit until nearly 2.5D downstream.

Additional resources

All PIV vector fields used in this work are stored in the ENCS database at WSU Vancouver. Access may be attained by contacting the corresponding author.

Declaration of Competing Interest

The authors declare that they have no known competing financial interests or personal relationships that could have appeared to influence the work reported in this paper.

CRediT authorship contribution statement

Bianca Viggiano: Formal analysis, Writing - original draft. Greg Sakradse: Formal analysis. Sarah Smith: Formal analysis. Rihana Mungin: Formal analysis. Pradeep Ramasubramanian: Formal analysis. Dan Ringle: Formal analysis. Kristin Travis: Formal analysis. Naseem Ali: Formal analysis, Writing - original draft. Stephen Solovitz: Conceptualization, Data curation, Funding acquisition, Investigation, Supervision, Writing - review & editing. Raúl Bayoán Cal: Conceptualization, Funding acquisition, Resources, Supervision, Writing - review & editing.

Acknowledgments

This work is supported by a grant (NSF-EAR-1346580) from the U.S. National Science Foundation.

Appendix A. Line integral convolution algorithm

The forward coordinate advection is computed as:

$$P_{i} = P_{i-1} + \frac{u(\lfloor P_{i-1} \rceil)}{||u(\lfloor P_{i-1} \rceil)||} \Delta s$$
(A.1)

where $u(\lfloor P_i \rceil)$ is the velocity vector for a given grid point, P_i , and Δs_i is the positive parametric distance along the unit velocity vector from P_i to the nearest cell edge. The asymmetric bracketing signifies that the grid point is rounded to the nearest integer. The cell edge is defined as:

$$s_e = \begin{cases} \infty & \text{if } u \text{ is parallel to } e \\ 0 & \text{if } \frac{|P_c| - P_c}{u_c} < 0 \\ \frac{|P_c| - P_c}{u_c} & \text{otherwise} \end{cases}$$
 (A.2)

where

for
$$(e, c) \in \begin{cases} (top, y) \\ (bottom, y) \\ (left, y) \\ (right, y) \end{cases}$$

and.

 $\Delta s_i = \min(s_{top}, s_{bottom}, s_{left}, s_{right}).$

The subscripts e and c represent the cell edge and the cell center, respectively. To maintain symmetry, the streamline is advected backwards by the negative of the vector direction, defined as:

$$P'_{i} = P'_{i-1} - \frac{u(\lfloor P'_{i-1} \rceil)}{||u(\lfloor P'_{i-1} \rceil))||} \Delta s'_{i-1}$$
(A.3)

where the prime denotes the negative direction counterparts.

The line interval convolution is completed by applying a convolution kernel along the direction of the streamlines presented above in the positive and negative directions. The intensity values of the output are correlated to the velocity field's local flow direction and can be expressed as:

$$G_{out}(x,y) = \frac{\sum_{i=0}^{l} G_{in}(\lfloor P_i \rceil) \lambda_i + \sum_{i=0}^{l'} G_{in}(\lfloor P_i' \rceil) \lambda_i'}{\sum_{i=0}^{l} \lambda_i + \sum_{i=0}^{l'} \lambda_i'},$$
(A.4)

where $G_{out}(x,y)$ is the output pixel value at (x,y), G_{in} is the input pixel value for a given point and l and l' are the convolution distances in the positive and negative directions respectively. The weighting variable, λ_i , is defined as

$$\lambda_i = \int_{s_i}^{s_i + \Delta s_i} \kappa(w) dw, \tag{A.5}$$

where $\kappa(w)$ is the convolution kernel, $s_0 = 0$, and Δs_i is the arc length between the point s_i and s_{i+1} along the streamline.

References

- [1] Woods AW. Turbulent plumes in nature. Annu Rev Fluid Mech 2010;42(1):391–412.
- [2] Hoult DP, Fay JA, Forney LJ. A theory of plume rise compared with field observations. J Air Pollut Control Assoc 1969;19(8):585–90.
- Koyaguchi T, Suzuki Y. Numerical simulations of turbulent flow in volcanic eruption clouds. Annual Report of the Earth Simulator Center 2008;2008.
- [4] McNeal JS, Freedland G, Mastin LG, Cal RB, Solovitz SA. Investigating the Accuracy of One-Dimensional Volcanic Plume Models using Laboratory Experiments and Field Data. Journal of Geophysical Research: Solid Earth 2019:124(11):11290-304.
- [5] Freedland GA, Eliason G, Solovitz SA, Cal RB. The role of turbulent inflow on the development of a round jet in cross-flow. International Journal of Heat and Fluid Flow 2020;84:108592.
- [6] Amielh M, Djeridane T, Anselmet F, Fulachier L. Velocity near-field of variable density turbulent jets. Int J Heat Mass Transf 1996;39(10):2149–64.
- [7] Kaminski E, Tait S, Carazzo G. Turbulent entrainment in jets with arbitrary buoyancy. J Fluid Mech 2005;526:361–76.

- [8] Suzuki YJ, Koyaguchi T, Ogawa M, Hachisu I. A numerical study of turbulent mixing in eruption clouds using a three-dimensional fluid dynamics model. J Geophys Res 2005;110:B08201.
- [9] Krug D, Chung D, Philip J, Marusic I. Global and local aspects of entrainment in temporal plumes. J Fluid Mech 2017;812:222–50.
- [10] Wang P, Fröhlich J, Michelassi V, Rodi W. Large-eddy simulation of variable-density turbulent axisymmetric jets. Int J Heat Fluid Flow 2008;29(3):654-64.
- [11] Gharbi A, Amielh M, Anselmet F. Experimental investigation of turbulence properties in the interface region of variable density jets. Phys Fluids 1995:7(10):2444–54.
- [12] Viggiano B, Dib T, Ali N, Mastin LG, Cal RB, Solovitz SA. Turbulence, entrainment and low-order description of a transitional variable-density jet. J Fluid Mech 2018;836:1009-49.
- [13] Gerashchenko S, Prestridge K. Density and velocity statistics in variable density turbulent mixing. J Turbul 2015;16(11):1011–35.
- [14] Wolf M, Lüthi B, Holzner M, Krug D, Kinzelbach W, Tsinober A. Investigations on the local entrainment velocity in a turbulent jet. Phys Fluids 2012;24(10):105110
- [15] Mandelbrot BB. The fractal geometry of nature, 1. WH Freeman New York; 1982.
- [16] Kolmogorov AN. The local structure of turbulence in incompressible viscous fluid for very large Reynolds numbers. In: Dokl. akad. nauk sssr, 30; 1941. p. 299–303.
- [17] Benzi R, Paladin G, Parisi G, Vulpiani A. On the multifractal nature of fully developed turbulence and chaotic systems. J Phys A 1984;17(18):3521.
- [18] Meneveau C, Sreenivasan KR. Simple multifractal cascade model for fully developed turbulence. Phys Rev Lett 1987;59(13):1424.
- [19] Russell DA, Hanson JD, Ott E. Dimension of strange attractors. Phys Rev Lett 1980:45(14):1175.
- [20] Pentland AP. Fractal-based description of natural scenes. IEEE Trans Pattern Anal Mach Intell 1984(6):661–74.
- [21] Lopes R, Betrouni N. Fractal and multifractal analysis: a review. Med Image Anal 2009;13(4):634–49.
- [22] Eke A, Herman P, Bassingthwaighte J, Raymond G, Percival D, Cannon M, et al. Physiological time series: distinguishing fractal noises from motions. Pflügers Arch 2000;439(4):403–15.
- [23] Jaffard S, Lashermes B, Abry P. Wavelet leaders in multifractal analysis. In: Wavelet analysis and applications. Springer; 2006. p. 201–46.
- [24] Lane-Serff GF. Investigation of the fractal structure of jets and plumes. J Fluid Mech 1993;249:521–34.
- [25] Sykes RI, Gabruk RS. Fractal representation of turbulent dispersing plumes. J Appl Meteorol 1994;33(6):721–32.
- [26] Seo Y, Lyu S. Multifractal characteristics of the jet turbulent intensity depending on the outfall nozzle geometry. Stoch Environ Res Risk Assess 2016;30(2):653–64.
- [27] López P, Tarquis AM, Matulka A, Skadden B, Redondo JM. Multiscaling properties on sequences of turbulent plumes images. Chaos Solitons Fractals 2017;105:128–36.
- [28] Kadum H, Rockel S, Hölling M, Peinke J, Cal RB. Wind turbine wake intermittency dependence on turbulence intensity and pitch motion. ournal of Renewable and Sustainable Energy 2019;11(5):053302.
- [29] KadumKadum, Hawwa and Rockel, Stanislav and Viggiano, Bianca and Dib, Tamara and Hölling, Michael and Chevillard, Laurent and Cal, Raúl Bayoán H, Rockel S, Viggiano B, Tamara D, Hölling M, Chevillard L, Cal RB. Assessing intermittency characteristics via cumulant analysis of floating wind turbines wakes. Journal of Renewable and Sustainable Energy 2021;13(1):013302.
- [30] Mukli P, Nagy Z, Eke A. Multifractal formalism by enforcing the universal behavior of scaling functions. Phys A 2015;417:150–67.

- [31] Ali N, Cal RB. Scale evolution, intermittency and fluctuation relations in the near-wake of a wind turbine array. Chaos Solitons Fractals 2019:119:215–29.
- [32] Ali N, Fuchs A, Neunaber I, Peinke J, Cal RB. Multi-scale/fractal processes in the wake of a wind turbine array boundary layer. J Turbul 2019;20(2):93–120.
- [33] Ali N, Kadum HF, Cal RB. Focused-based multifractal analysis of the wake in a wind turbine array utilizing proper orthogonal decomposition. Journal of Renewable and Sustainable Energy. AIP Publishing LLC; 2016. p. 063306.
- [34] Keylock CJ. A criterion for delimiting active periods within turbulent flows. Geophys Res Lett 2008;35(11).
- [35] Bogard DG, Tiederman WG. Burst detection with single-point velocity measurements. J Fluid Mech 1986;162:389-413.
- [36] Katul G, Poggi D, Cava D, Finnigan J. The relative importance of ejections and sweeps to momentum transfer in the atmospheric boundary layer. Bound-Layer Meteorol 2006;120(3):367–75.
- [37] Hamilton N, Suk Kang H, Meneveau C, Cal RB. Statistical analysis of kinetic energy entrainment in a model wind turbine array boundary layer. J Renew Sustain Energy 2012;4(6):063105.
- [38] Keylock CJ, Nishimura K, Peinke J. A classification scheme for turbulence based on the velocity-intermittency structure with an application to near-wall flow and with implications for bed load transport. J Geophys Res 2012;117:F01037.
- [39] Camp EH, Cal RB. Low-dimensional representations and anisotropy of model rotor versus porous disk wind turbine arrays. Phys. Rev. Fluids 2019;4(2):024610. doi:10.1103/PhysRevFluids.4.024610.
- [40] Camp EH, Cal RB. Mean kinetic energy transport and event classification in a model wind turbine array versus an array of porous disks: Energy budget and octant analysis. Phys. Rev. Fluids 2016;1(4):044404.
- [41] Ali N, Hamilton N, Calaf M, Cal RB, et al. Turbulence kinetic energy budget and conditional sampling of momentum, scalar, and intermittency fluxes in thermally stratified wind farms. Journal of Turbulence 2019;20(1):32–63.
- [42] Herzog M, Oberhuber JM, Graf H-F. A prognostic turbulence scheme for the nonhydrostatic plume model atham. J Atmos Sci 2003;60(22):2783–96.
- [43] Cabral B, Leedom LC. Imaging vector fields using line integral convolution. In: Proceedings of the 20th annual conference on computer graphics and interactive techniques. ACM; 1993. p. 263–70.
- [44] Forssell LK, Cohen SD. Using line integral convolution for flow visualization: curvilinear grids, variable-speed animation, and unsteady flows. IEEE Trans Vis Comput Graph 1995;1(2):133–41.
- [45] Urness T, Interrante V, Marusic I, Longmire E, Ganapathisubramani B. Effectively visualizing multi-valued flow data using color and texture. In: Proceedings of the 14th IEEE visualization 2003 (VIS'03). IEEE Computer Society; 2003. p. 16
- [46] Matvienko V, Krüger J. Explicit frequency control for high-quality texture-based flow visualization. In: Scientific visualization conference (SciVis). IEEE; 2015. p. 41–8.
- [47] Kays WM, Crawford ME. Convective heat and mass transfer. 2nd ed. Mc-Graw-Hill, New York; 1993.
- [48] Melling A. Tracer particles and seeding for particle image velocimetry. Meas Sci Technol 1997;8(12):1406.
- [49] Raffel M, Willert CE, Kompenhans J. Particle image velocimetry: a practical guide. Springer; 2013.
- [50] Han D. Study of turbulent nonpremixed jet flames using simultaneous measurements of velocity and CH distribution. Stanford University; 2001. Ph.D.
- [51] Mastin LG, Guffanti M, Servranckx R, Webley P, Barsotti S, Dean K, et al. A multidisciplinary effort to assign realistic source parameters to models of volcanic ash-cloud transport and dispersion during eruptions. J Volcanol Geotherm Res 2009;186(1-2):10-21.